International Journal of Hydrological and Environmental for Sustainability
Volume 5, Issue 3, 287-299.
e_ISSN: 2828-5050
https://www.journal.foundae.com/index.php/ijhes

Imaging Fault Gouge Zones along the Menanga Fault using Integrated Electrical Resistivity and Multi-frequency Ground Penetrating Radar in Pesawaran, Lampung, Indonesia

Rahmat Nawi Siregar*
Department of Physics,
Institut Teknologi Sumatera,
INDONESIA

Muhammad Ragil Setiawan
Department of Physics,
Institut Teknologi Sumatera,
INDONESIA

Bilal Al Farishi
Department of Geological Engineering,
Institut Teknologi Sumatera,
INDONESIA

Ikah Ning P Permanasari
Department of Physics,
Institut Teknologi Sumatera,
INDONESIA

Sofiana Herman
Department of Physics,
Institut Teknologi Sumatera,
INDONESIA

Denny Pratama
Department of Physics,
Institut Teknologi Sumatera,
INDONESIA

Devina Anggraini
Department of Physics,
Institut Teknologi Sumatera,
INDONESIA

Shofiya Nisfatul Laily
Department of Physics,
Institut Teknologi Sumatera,
INDONESIA

Monalisa Devinci Pardosi
Department of Physics,
Institut Teknologi Sumatera,
INDONESIA

***Correspondence: E-mail:** rahmat.siregar@fi.itera.ac.id

Article Info

Article history:

Received: February 10, 2026
Revised: July 29, 2026
Accepted: August 28, 2026

Abstract

Detecting fault gouge zones in poorly exposed fault systems is critical for understanding active deformation. The Menanga fault in Pesawaran (Lampung) revealed its activity during the 2021 swarm earthquake near Mt. Ratai at 1.5-4.5 km depth. Due to the limited exposure of the fault plane, geophysical imaging is applied to delineate subsurface structures. In this work, we conducted three survey lines using integrated geoelectric method and multi-frequency ground penetrating radar (50 MHz, 100 MHz, and 250 MHz) to investigate a clear image of Menanga fault zone. The electrical resistivity profiles revealed lateral discontinuities between relatively high-resistivity blocks separated by lower-to-intermediate resistivity materials, whereas the GPR profiles showed signal attenuation, chaotic radar facies, and discontinuous reflectors associated with structurally disturbed zones. Fault-related deformation zones were characterized by resistivity contrasts relative to adjacent high-resistivity blocks, together with low-amplitude, chaotic, and discontinuous GPR reflections. The clearest anomaly occurs at approximately 96 m offset along Line 1, where the subsurface discontinuity coincides with an exposed fault zone. Line 2 shows multiple fault-related discontinuities, whereas Line 3 exhibits an inferred deformation zone without clear surface exposure. Overall, the integration of electrical resistivity and multi-frequency GPR effectively delineates the shallow architecture of the Menanga Fault and provides geophysical evidence of fault-related deformation consistent with previous seismic and geomorphological studies.

Keywords: fault gouge, electrical resistivity method, ground penetrating radar, Menanga fault. Pesawaran

To cite this article: Siregar, R. N., Setiawan, M. R., Al Farishi, B., Permanasari, I. N. P., Herman, S., Pratama, D., Anggraini, D., Laily, S. N., & Pardosi, M. D. (2026). Imaging Fault Gouge Zones along the Menanga Fault using Integrated Electrical Resistivity and Multi-frequency Ground Penetrating Radar in Pesawaran, Lampung, Indonesia. *International Journal of Hydrological and Environmental for Sustainability, 5*(3), 287-299. https://doi.org/10.58524/ijhes.v5i3.1009

INTRODUCTION

Sumatra Island is located on one of the world's most seismically active zones, controlled by the subduction of Indo-Australian plate beneath the Eurasian plate and the major Great Sumatran Fault (GSF) system (Sieh & Natawidjaja, 2000). The GSF is a major strike-slip fault system which extends along the entire length of Sumatera, stretching from Aceh in the north to Lampung in the south (Sieh & Natawidjaja, 2000). Historically, this active tectonic setting has been responsible for massive seismic events such as the 1994 Liwa Earthquake (Magnitude 6.8) (Duquesnoy et al., 1996). While extensive research has focused on the main GSF strike-slip movement, minor and local fault systems also possess significant seismic potential like the 2021 swarm earthquake which triggered by the activity of the Menanga fault in Pesawaran region (Lampung) (Nurfitriana et al., 2021; Hendrawan et al., 2023).

Menanga fault is a NW-SE fault trend which related to the presence of Mt. Ratai, a dominant control of Pesawaran geological setting (Nurfitriana et al., 2022; Hendrawan et al., 2023). The geological structures were formed during the subduction on Palaeozoic which led to the formation of Undifferentiated Gunung Kasih Complex with mainly methamorphic rocks such as pelitic schist and minor gneiss. During the Early Cretaceous, the Menanga formation was deposited, consisting of alternating shale and claystone with basalt, intercalations of chert, and lenses of formation. This formation kept evolving and by the Paleocene, Tarahan Formation and Sabu Formation as a product of Mt Ratai volcanic rocks. The Hulusimpang formation was then developed in Oligocene with massive andesite basalt lava, tuff, and volcanic breccia with lenses of limestone. The Pleistocene period marked the formation of the Pesawaran Young Volcanic Deposits, which were subsequently covered by Holocene alluvium (Mangga et al., 2010).

The geological framework of the study area consists of metamorphic, sedimentary, volcanic, and unconsolidated units that may produce contrasting geophysical responses (Mangga et al., 2010). The oldest unit is the Gunung Kasih Complex, dominated by schist and minor gneiss, followed by the Menanga Formation consisting mainly of shale, claystone, basalt, and chert (Mangga et al., 2010). Younger units include the Tarahan and Sabu formations, volcanic rocks of the Hulusimpang Formation, Pleistocene volcanic deposits, and Holocene alluvium (Mangga et al., 2010). Rather than their stratigraphic ages alone, the physical contrasts among these lithologies are important for interpreting the geophysical data (Nevedrova et al., 2017; Monge-Cerda et al., 2024). Relatively compact volcanic or carbonate rocks are expected to produce higher resistivity and more coherent radar reflections when less weathered, whereas clay-rich, fractured, weathered, or water-saturated materials generally produce lower resistivity and stronger GPR attenuation (Lockner & Byerlee, 1985; Pauselli et al., 2010; Galli et al., 2014; Aliyannezhadi et al., 2020). Consequently, fault-related deformation zones are interpreted from the combined occurrence of lateral resistivity contrasts, disruption of resistive blocks, and attenuated or chaotic radar reflections rather than from a single resistivity range (Galli et al., 2014; Nevedrova et al., 2017; Sellmann et al., 2022; Monge-Cerda et al., 2024; Famiglietti et al., 2025).

These lithological variations are particularly relevant to the three survey lines (**Figure 1**). Line 1 crosses a fault exposure within a predominantly volcanic setting, where relatively resistive blocks are separated by more conductive disturbed materials. Line 2 crosses the limestone hill area, where high-resistivity carbonate rocks provide a strong contrast with fractured and weathered zones. Line 3 lies close to the boundary between the Tarahan, Sabu, and Way Galih units, making the distinction between lithological contacts and fault-related discontinuities more uncertain (Mangga et al., 2010).

One of the most interesting geological events on Menanga Fault is the 2021 swarm earthquake at 1.5-4.5 km depth with 22 earthquake events, related to shallow crustal activity (Nurfitriana et al., 2021). Nurfitriana et al (2021) delineated the structural trend by relocating earthquake hypocentre which precisely located on the inferred Menanga fault line. Thus, the relocation analysis of hypocentres conclude that the Pesawaran swarm earthquake was triggered by the active Menanga Fault. Nurfitriana et al (2022) later performed gravity method in identifying the existence of Menanga fault. The study revealed that Menanga fault has NW-SE orientation and likely crosses the summit of Mt. Ratai. Hendrawan et al (2023) confirmed the presence of major active tectonic process of Menanga Fault with geomorphic indices. The study also reported that the landform formation in the research area was not only affected by Menanga fault, but also controlled by the growth of Mt. Ratai.

The occurrence of shallow seismicity is particularly important for local seismic hazard because deformation on shallow crustal faults may produce stronger near-surface ground motion and may affect populated areas located close to the fault trace (Nurfitriana et al., 2021; Hendrawan et al., 2023). However, the shallow geometry, continuity, and internal deformation structure of the Menanga Fault remain poorly constrained. Therefore, detailed near-surface geophysical imaging is required to identify fault-related discontinuities and deformation zones and to better characterize the structural framework associated with this seismically active area (Galli et al., 2014; Aliyannezhadi et al., 2020; Sellmann et al., 2022; Monge-Cerda et al., 2024; Famiglietti et al., 2025).

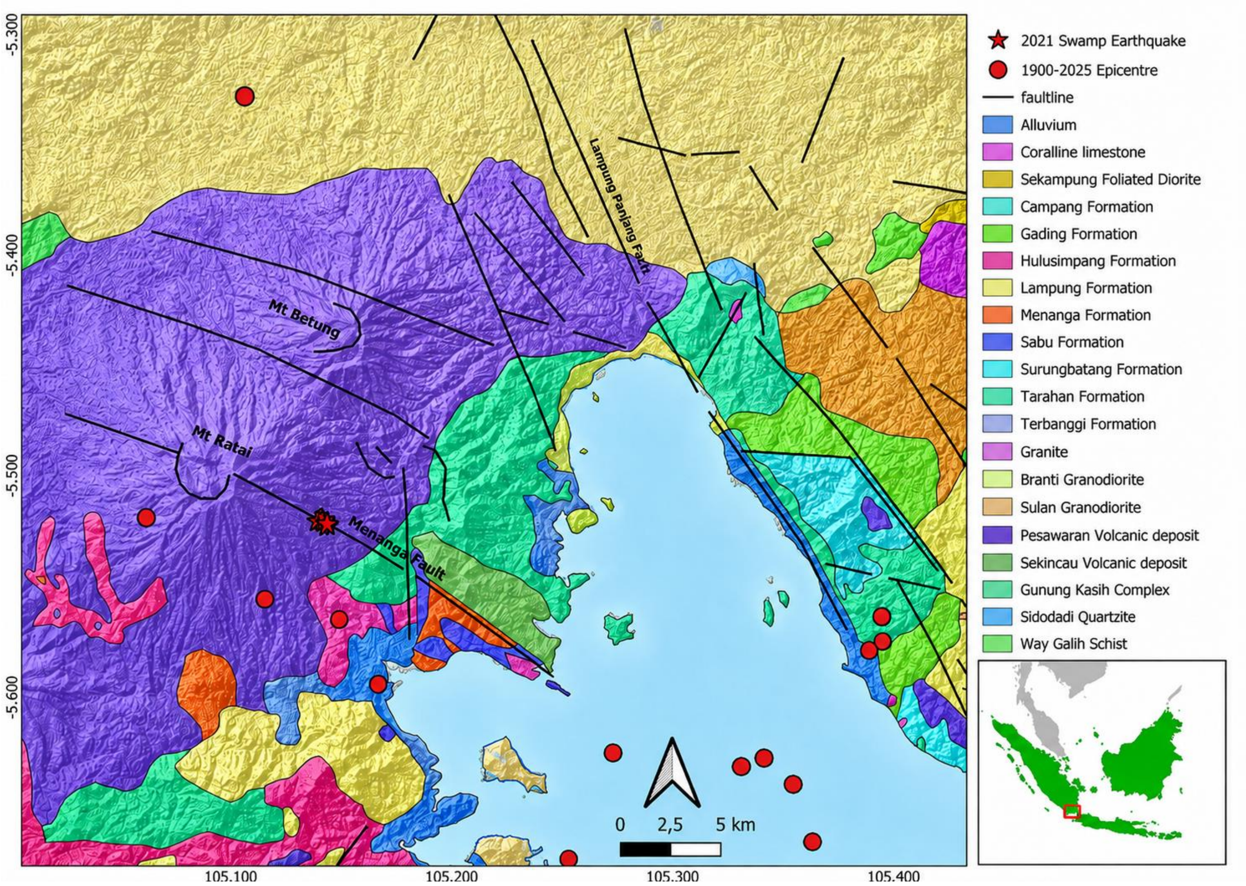

Figure 1. Geological map of Lampung indicate the main Lampung-Panjang fault based on Mangga et al. (1993). The 2021 swarm earthquakes are plotted around Menanga Fault. The red dot indicates the 1900-2025 earthquake history around research area

One of the most crucial indicators in identifying active fault is the presence of fault gouge which generally consisted of highly saturated, clay-rich and rupture materials. Relative movement along a fault plane is responsible for the occurrence of fault gouge (Hirata et al., 2017; Argante et al., 2022). The fractures formed are subsequently filled with loose materials such as clay, fine sediments and water penetration which can be easily observed in the outcrop surface. However, tracing its continuity at depth in a location with no clear fault outcrop is more challenging, requiring powerful subsurface mapping methods which capable of both lithological contrasts and structural fractures.

Thus, in this study we performed two methods for detecting the continuation of fault at depth: the integration of geoelectric and multi-frequency ground penetrating radar (GPR). Resistivity profile from geoelectric method is highly sensitive to variations in clay and water-rich zones, make it effective for delineating the fault plane (Lockner & Byerlee, 1985; Galli et al., 2014; Nevedrova et al., 2017; Adni Pesma & Sitanggang, 2024; Monge-Cerda et al., 2024). Meanwhile, GPR offers high resolution image of shallow subsurface, weaken radar amplitude and chaotic zones which associated with fractured and deformed material (Pauselli et al., 2010; Aliyannezhadi et al., 2020; Sellmann et al., 2022; Famiglietti et al., 2025). Three frequencies of radar will be carried out in this research: (1) 50 MHz penetrates deeper (up to 32 m) to capture broad structural features, (2) 100 MHz for 15 m depth and (3) 250 MHz assigns the highest resolution in 8 m depth. By integrating these methos, a comprehensive pictures of fault geometry will detect the gouge zones and their continuity beneath the surface, thus providing direct geophysical evidence of active faulting.

METHOD

This research is part of a structured investigation around Padang Cerming and Way Ratai Districts in Pesawaran Regency, Lampung Province, Indonesia. These districts lie within the tectonically active margin of the Semangko fault, where the Menanga fault has been inferred from geomorphological anomalies but remains poorly explored. To address this, the research investigates the presence of Menanga fault by integrating multichannel geoelectric resistivity and varied-frequency ground penetrating (**Figure 2**).

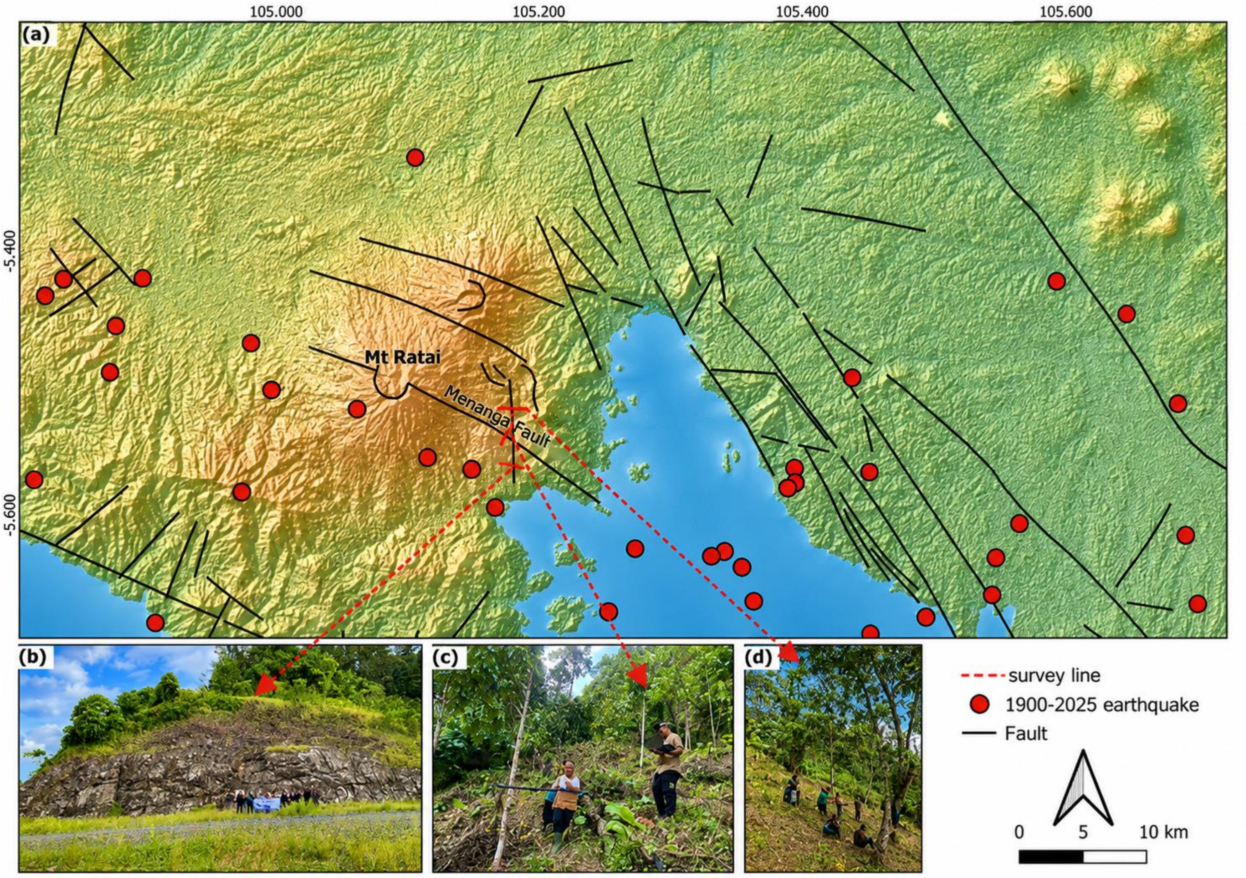

Figure 2. Regional geomorpholigcal and structural map based on (a) 30-m digital elevation map and integrated geophysical survey of (b) Line 1 in Menanga hill, (c) Line 2, and (d) Line 3

The preliminary data was based on regional geological information, field survey and secondary data; published maps and previous geological studies of Pesawaran area, which provided guidance for designing geoelectric survey. The locations, survey geometry, geological settings, target structures, and main acquisition parameters of the three survey lines are summarized in **Table 1**. The geoelectric method was performed to investigate subsurface resistivity variations due to lithological differences and the presence of structural discontinuities which are generally found around active faults. In this study, the Wenner configuration was employed using an IRES T300F resistivity meter with 46 electrodes deployed at a uniform spacing of 4 m, resulting in an electrode spread of 180 m along each approximately 200 m survey line. The apparent resistivity data were inverted into two-dimensional subsurface resistivity models with topography incorporated into the inversion. The inversion converged after 9, 13, and 12 iterations for Lines 1, 2, and 3, respectively, with final absolute errors of 9.6%, 9.5%, and 9.6%. The resulting models provided subsurface imaging to approximately 25–30 m below the local ground surface. For consistency, all resistivity sections are presented in Ωm using the same resistivity scale, ranging from 10.7 to 1459 Ωm

The geoelectric lines were 180 meter long and oriented perpendicular to the inferred fault, ensuring that resistivity profiles intersected the fault zones, thereby maximizing sensitivity to lateral contrasts and enhancing the visibility of resistivity anomalies associated with fractured zones and fault gouge. Raw resistivity measurements obtained from the multichannel system were first corrected for electrode spacing and field geometry. The apparent resistivity data were processed and inverted into two-dimensional resistivity models of the subsurface using RES2DINV software with smoothness-constrained least-squares inversion approach. The inversion results were interpreted in terms of low-resistivity zones potentially corresponding to clay-rich damaged zones and saturated fractured rocks, while higher resistivity zones associated with intact bedrock or less weathered materials.

Table 1. Summary of the electrical resistivity and multi-frequency GPR survey lines across the Menanga Fault area

Survey Line	Location	Start Coordinate	End Coordinate	Line Length (m)	Orientation	Elevation range	Geological Features	GPR Frequencies
Line 1	Menanga Hill	05°34.378′ S, 105°11.394′ E	05°34.378′ S, 105°11.288′ E	180	E-W	21-32	Dominantly volcanic/basaltic rocks; exposed fault zone	50, 100, 250 MHz
Line 2	Dantar	05°33.598′ S, 105°10.629′ E	05°33.696′ S, 105°10.660′ E	180	NE-SW	86-112	Limestone-dominated hill with fractured/weathered zones	50, 100, 250 MHz
Line 3	Batu Menyan Hill	05°32.964′ S, 105°10.972′ E	05°32.919′ S, 105°11.050′ E	180	E-W	81-101	Boundary of Tarahan Formation, Sabu Formation, and Way Galih Schis	50, 100, 250 MHz

As geoelectric method reveals the resistivity contrasts and broader lithological variations, its resolution is limited in capturing fine-scale discontinuities. Therefore, Ground Penetrating Radar (GPR) was applied to enhance higher-resolution profiles of fractured zones, fault gouge, and lithological boundaries which may not be distinctly resolved by resistivity data (Pauselli et al., 2010; Aliyannezhadi et al., 2020; Lei et al., 2022; Famiglietti et al., 2025). Furthermore, in this research we employed three different frequencies of radar antenna to obtain a multi-scale subsurface information, enabling both shallow high-resolution of fractured zones and deeper detection of fault gouge and lithological discontinuities.

The GPR method was acquired using the Goldie-21 Compact Finder systems with three frequencies: (1) 50 MHZ for detecting near-surface (3-10 m) fractures and sediment layering, (2) 100 MHz for identifying structural transitions and deformation zones, and (3) 25 MHz for exploring deeper fault features. Data were acquired at a trace interval of 1 m with 512 samples per trace. Sampling intervals of 1.0, 0.5, and 0.25 ns were used for the 50, 100, and 250 MHz data, respectively, corresponding to recording time windows of approximately 512, 256, and 128 ns. Time-to-depth conversion was performed using an assumed electromagnetic-wave velocity of 0.125 m ns^{-1}, resulting in approximate maximum depth windows of 32, 16, and 8 m for the 50, 100, and 250 MHz profiles, respectively.

The GPR processing workflow consisted of time-zero correction, dewow filtering, gain adjustment, band-pass filtering, migration, and Hilbert-transform envelope analysis. Time-zero correction was first applied to align the first arrivals and establish a consistent temporal reference among traces. Dewow filtering was then used to remove low-frequency components and baseline drift, followed by gain adjustment to compensate for amplitude decay with increasing travel time. Frequency-dependent band-pass filtering was applied according to the bandwidth of the 50, 100, and 250 MHz antennas to suppress frequencies outside the useful signal range. Migration was performed using an assumed electromagnetic-wave velocity of 0.125 m ns^{-1} to reposition dipping and diffracted reflections toward their apparent subsurface locations. In addition, Hilbert transform envelope filtering was employed to emphasize reflection amplitudes (Jabbar et al., 2024; Li et al., 2025), thereby improving the visibility of fractured zones, fault gouge and lithological discontinuities.

RESULTS AND DISCUSSION

The integrated interpretation of the three survey lines was based on the spatial coincidence of multiple geological and geophysical indicators rather than on a single resistivity or GPR anomaly. Fault-related deformation zones were identified by: (1) low- to intermediate-resistivity zones relative to adjacent more resistive blocks, (2) lateral discontinuity or apparent displacement of resistivity structures, (3) truncation or disruption of radar reflectors, (4) chaotic radar facies, (5) low-amplitude responses or signal attenuation, and, where available, (6) spatial correspondence with mapped fault exposures or structural lineaments. Fault gouge was interpreted with greater confidence where several of these indicators occurred simultaneously and were consistent with field geological evidence.

However, low resistivity, chaotic reflections, and radar attenuation are not uniquely diagnostic of fault gouge. Similar geophysical responses may result from water-saturated or clay-rich materials, intensive weathering, lithological contacts, roots, boulders, or local topographic effects. Therefore, isolated anomalies were not interpreted as fault gouge unless they were supported by complementary resistivity and GPR signatures and their geological or structural context. This integrated criterion is particularly important for distinguishing the well-constrained fault zone at Line 1 from the more uncertain interpretations at Lines 2 and 3.

The details interpreted profiles are discussed with particular attention to subsurface anomalies, fault-related signatures, and distinct lithological features. Instead of discussing each method separately, the analysis integrates geoelectric and GPR data coverage to delineate structural discontinuities and deformation zone associated with the inferred Menanga fault. To get a better result, the geological evidence from Menanga Hill, which actually give the Menanga fault's name, was used to control the interpretation. The line 1 survey was conducted on Menanga Hill, extending for a total length of 200 m across the slope. To maximize the structural visibility and more valid interpretation, the midpoint of the line (around 100 m) was strategically positioned directly over the clearly exposed Menanga fault outcrop as can be seen in **Figure 3a**.

Line 1 – Menanga Hill

The 200m-long resistivity profile was carried out with E-W orientation from the lower topographic surface of Menanga Hill. The resistivity profile shows a clear discontinuity that parallel with the structural features observed in **Figure 3a** as can be observed in the midpoint of the line (96 m). The stratigraphic layers show discontinue pattern, indicating one block moved downward relative to the other due to normal fault (white line). This fault can be detected through resistivity inversion in **Figure 3b**, where two high resistivity zones interpreted as basalt rocks (723 -1459 Ωm) are separated in 96-meter offset. This discontinuity is parallel with fault plane outcrop which strengthening the proof of relative movement of each block in deeper subsurface.

Between the two separated high resistivities, intermediate resistivity range (around 358 – 723 Ωm) which shown with brown colour in resistivity profile are interpreted as disturbance zone and fractured material. The presence of this zone is a key indicator for fault detection in reflecting the mechanical damage along the fault plane. The energy generated from active fault increases the shear stress, leading to brecciation, fracturing and deformation (Hirata et al., 2017; Argante et al., 2022). The porosity and permeability of fractured layer allow water to penetrate the deformation zones. This mechanism explains why the intermediate resistivity zone is found around the high resistivity zone. The lower resistivity (10.7 – 43.6 Ωm) discontinuities were also found in several location which represent disruptive material, water-saturated and intensive weathering.

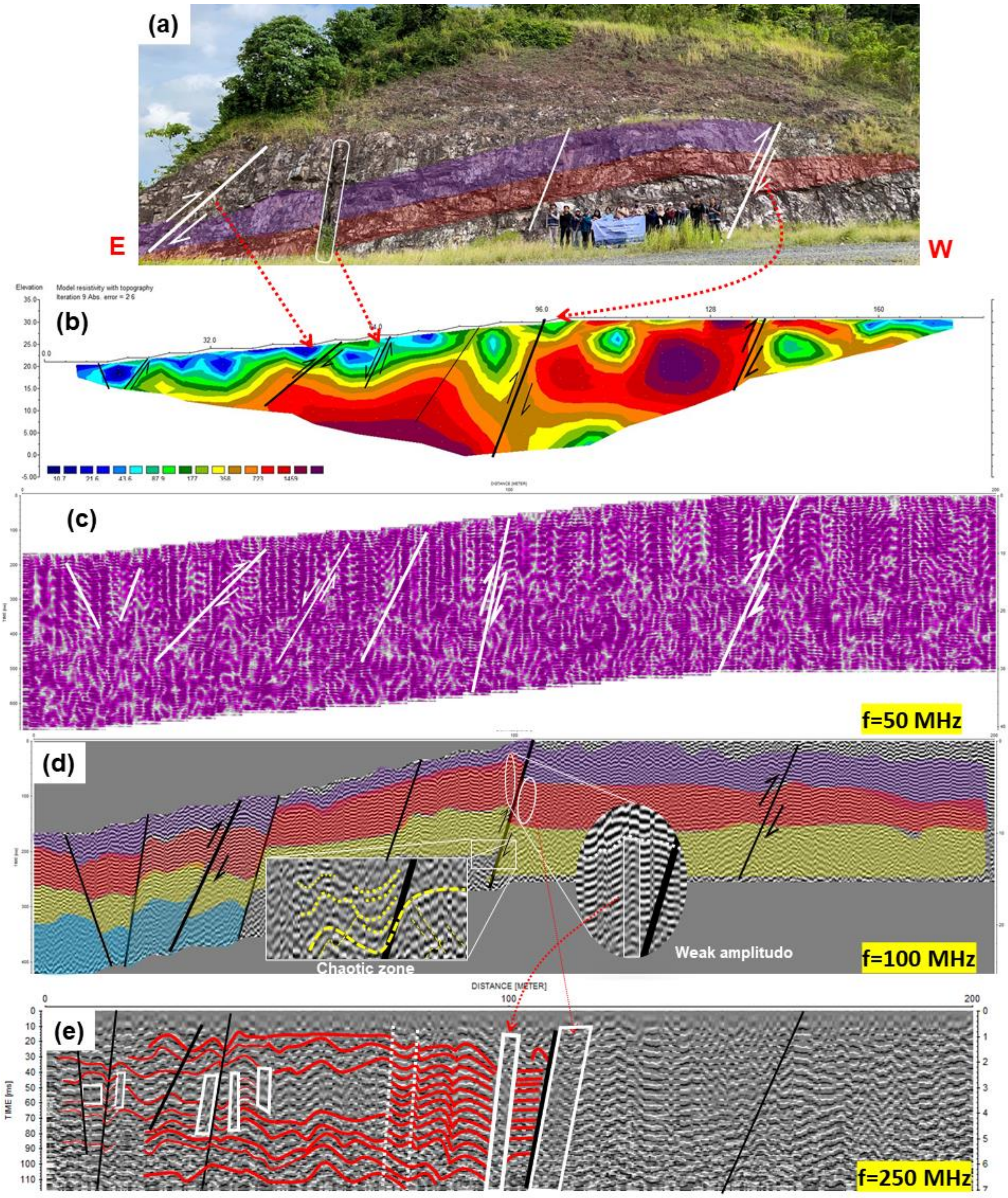

Figure 3. Integrated survey of Line 1 on Menanga hill fault zone: (a) interpreted outcrop showing surface faulting, (b) resistivity variation profile, (c-e) GPR profiles (50, 100 and 250 MHz) reveal decreasing depth but increasing resolution

Furthermore, radargram profiles from three different frequencies were used to clarify the detailed structure of disturbed zones. The 50 MHz radargram profiles in **Figure 3c** was processed with Hilbert transform to confirm reflection signal amplitudes to 32 m depth. The Hilbert transform show the contrast refection between basalt and disturbed material. The disturbed zone in 96-meter offset previously discussed as the intermediate resistivity can be identified as weak and irregular amplitudes to 32 m depth. The penetration of radar wave in this zone is scattered, discontinue, and low intensity which indicate the intense weathering and fracturing. At a depth of 20 m and distance from 8 to 100 m, the same pattern can be observed which previously indicate the presence of fault zone in geoelectric profile. Thus, the 50 MHz radargram with Hilbert transform provides clear evidence of internal structure of Menanga fault from 0 to 30-meter depth.

The higher resolution of shallower subsurface can be explored with 100 MHz radargram profile (**Figure 3d**). At a distance of 90-100 m and 0-5 m depth, the amplitudes were significantly attenuated around the gault gouge. Based on resistivity profile, this layer is identified with intermediate resistivity (87 – 177 Ωm) which indicates an increase in water content. Physically, more saturated water will increase the dielectric constant and later reduce the velocity of radar. At 5-10 m depth, a stronger reflection can be identified below low amplitude section, indicating the presence between two layers (interface). Moreover, at 12 m depth, the chaotic and irregular zone shows high heterogeneity material which consists of loose, fine-grainer and water-saturated material. This material is an indicator of fault gouge indicator which generally formed in shallow fault zones with brittle deformation mechanism (Hirata et al., 2017; Argante et al., 2022).

The 250 MHz radargram (**Figure 3e**) further clarifies the detail of chaotic and weak amplitude in the 5-10 m depth. The topographical correction was not applied in this profile to get a better image of subsurface information. As **Figure 3d** present the disturbed zones as weak amplitude, the 250 MHz profiles show much sharper and clearer discontinuity. Red line and white box enhance the resolution of highly disrupted area, discontinue and low energy reflectors along the fault plane. Meanwhile, continuous layers can be identified from 90-100 m with coherent red line which marked from dashed white line. The continuous radar reflections were generated based on high dielectric constant of these layers which sharply contrast the attenuated amplitudes observed in the fault gouge.

Line 2- Dantar

Fault outcrop was identified around limestone hill as can be inferred from **Figure 4a**. Due to the highly rugged topography of the research site, the fault outcrop could not be positioned in the midpoint of the geoelectric line. Similar to Line 1, Line 2 was conducted with 4-m electrode spacing but with different S-N orientation. Several visible fault features can be identified from resistivity profile in **Figure 4b**. At a distance of 48-60 m, two intermediate resistivity features (25-66 Ωm) show discontinuous layers which indicating faulting zones at 110-95 m of elevation. The 1087 Ωm layer can be identified from 32 to 64 m distance which inferred as the limestone formation which dominantly govern the area. At a distance of 108-116 m, visible fractures can be observed with the separation of two high resistivity block. This suspected fracture zone is a continuation of the observed fault on limestone hill. Visible fractures and layer displacements are also observed in 128 m and 160 m at shallower depth and lower resistivity range which record the weathered and discontinuous rock surfaces.

The fractures are clearly visible when Hilbert transform was applied in a 50 MHz radargram profile at 64 m, 110m, 128 and 160 m offset. The most distinct anomalies from **Figure 4c** were captured at 100-110 m offset and 120-160 m at 30-50 m depth. Wide range of low amplitudes were distinctly recognized below the fault plane, indicating the presence of clay-rich, more saturated and disturbed material. These anomalies were then inspected with 100 MHz of radar antenna which give the radargram profile in **Figure 4d**. The coherent strong reflector along the profile is suspected is the interface of different lithological units (Pauselli et al., 2010; Aliyannezhadi et al., 2020; Lei et al., 2022). The disturbance zones and fractures materials which previously presented were marked in the insert figure of **Figure 4d**. The chaotic zone and weak amplitude were observed in the shallower depth (around 10 m) which can be inferred as the fault gouge (Pauselli et al., 2010; Sellmann et al., 2022; Famiglietti et al., 2025). The higher resolution stratigraphy with 250 MHz frequency (**Figure 4e**) shows some coherent and continue reflector (blue shaded) from 0 to 7 m depth which correspond to layers with higher dielectric constant and typically higher resistivity (Galli et al., 2014; Lei et al., 2022). Resistivity section show high resistivity at shallow depth in around 100 m offset, confirming the less weathered zone. But the damage zones are also easily found around the fault plane, defining the fault gouge boundaries from the more compact layer (Galli et al., 2014; Sellmann et al., 2022; Argante et al., 2022).

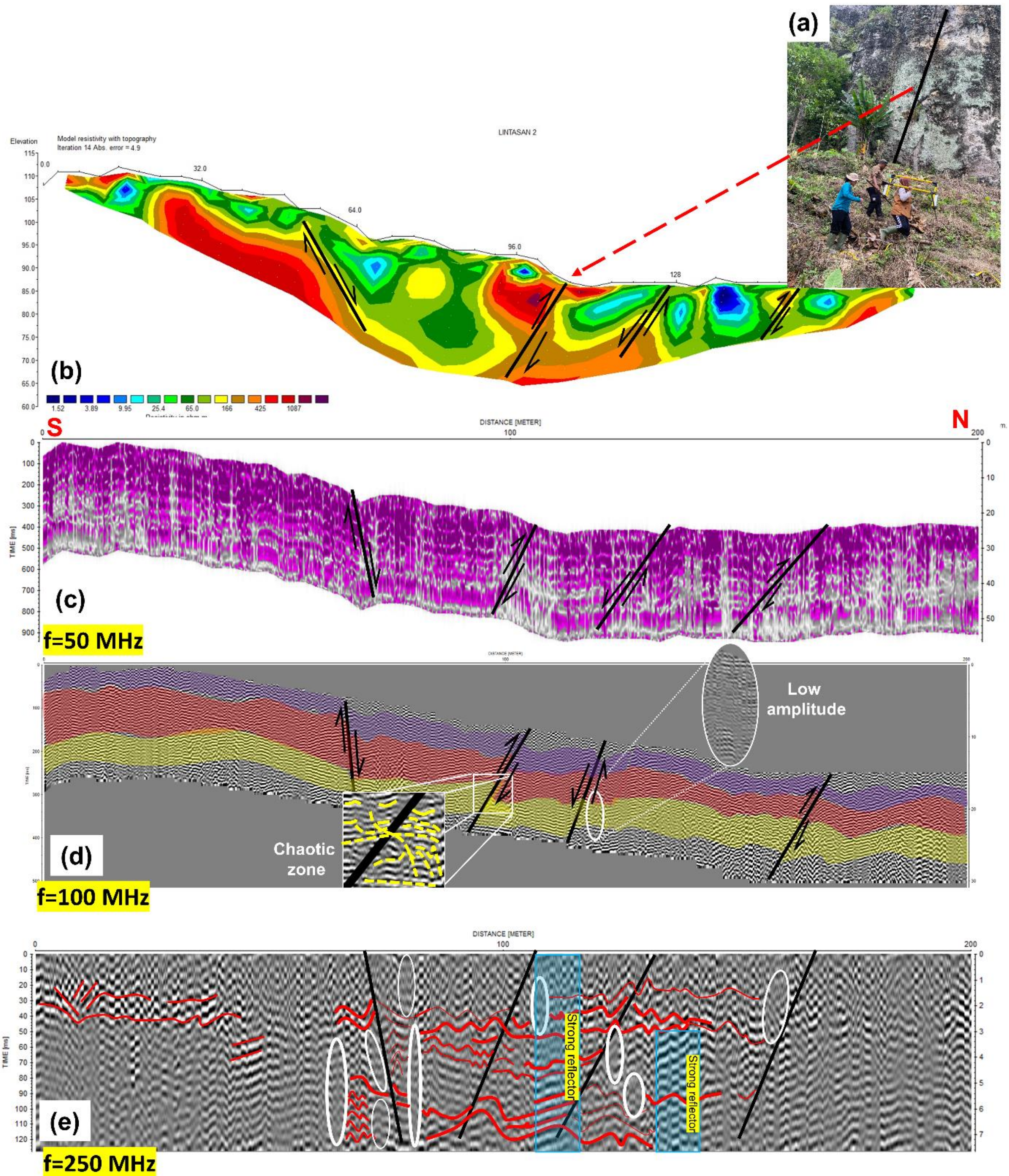

Figure 4. Complete geophysical survey of Line 2: (a) field evidence of Menanga fault, (b) 200-m resistivity profile and (c-e) radargram profiles with different frequencies

Line 3 – Batu Menyan Hill

The investigation along Line 3 at Batu Menyan Hill was conducted across sloped terrain as shown in **Figure 5a**. Unlike Line 1 and Line 2, there was no clear fault outcrops were visibly exposed. This location is located on boundary zone of three distinct lithological formations: Tarahan formation (welded tuff, breccia) to the west, Sabu formation (alternating conglomerate breccia with sandstone) to the south, and Way Galih Schist formation to the east. The resistivity section with 4.6 % of error shows relative movement of two high resistivity (1459 Ωm) blocks in 90-110 m offset and 20 m depth. This feature can be observed in **Figure 5c**, where 50 MHz section provides the weak amplitude signature which indicate strong attenuation at 10-20 m depth.

The 100 MHz radargram (**Figure 5d**) shows a more detailed low amplitude at 10-15 m depth and chaotic zone at 2-5 m depth. A distinct chaotic zone indicates fault gouge with clay enrichment and fluid saturation which decrease the amplitude of radar wave. Furthermore, the coherent and strong reflectors are mainly detected along the 1-3 m depth of 250 MHz profile as shown in **Figure 5e**. But from 50 to 150 m offset at >4 m depth the coherent reflectors change to fragmented and discontinuous layer, inferring the gouge boundary. The more detailed chaotic zone is giving a more real image of fault gouge which often consisted of water-saturated material, fragmented rocks and fine-grained clay, which reduce the radar wave penetration (Pauselli et al., 2010; Argante et al., 2022; Sellmann et al., 2022; Famiglietti et al., 2025).

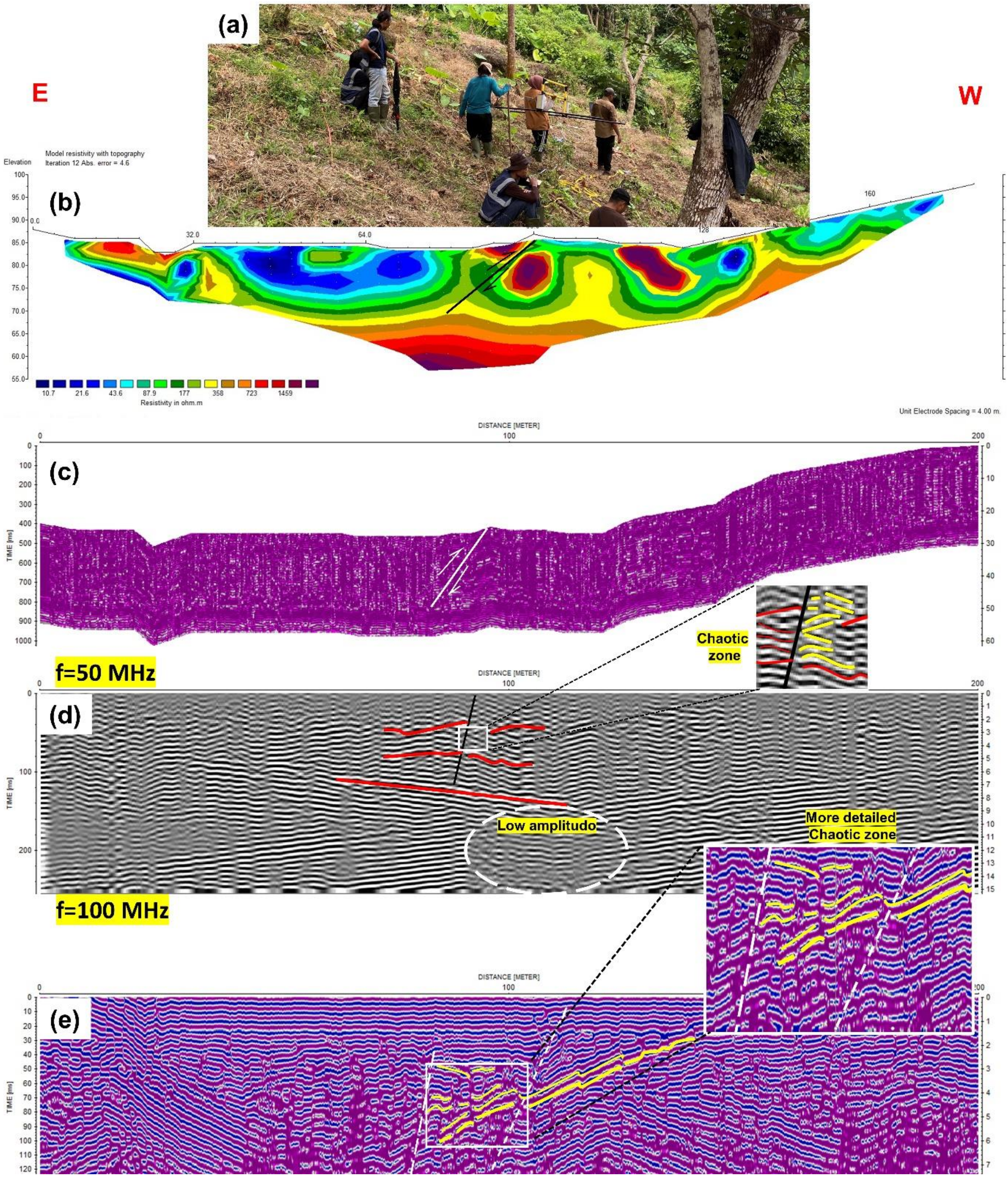

Figure 5. The inferred Menanga fault from Line 3 showing (a) Batu Menyan hill, (b) resistivity section, lateral profile of different radar frequencies from (c) 50 MHz, (d) 100 MHz and (e) 250 MHz.

CONCLUSION

This study demonstrates the integration electrical resistivity and multi-frequency GPR for imaging the shallow structure of the Menanga Fault zone. Along Line 1 at Menanga Hill, the most strongly constrained fault-related zone was identified at approximately 96 m along the profile, where the geophysical anomaly coincides with an exposed fault plane. The zone is characterized by lateral resistivity contrasts between relatively high-resistivity blocks and lower- to intermediate-resistivity disturbed materials, together with low-amplitude, chaotic, and discontinuous GPR reflections. Along Line 2 at Dantar, several resistivity discontinuities and attenuated radar responses indicate multiple fracture and possible gouge zones associated with the fault exposure near the limestone hill. In contrast, Line 3 at Batu Menyan Hill shows an inferred fault-related deformation zone defined by discontinuity of relatively high-resistivity blocks and corresponding low-amplitude and chaotic GPR responses, although the interpretation remains less constrained because no clear fault outcrop is exposed.

Overall, the most reliable indicators of fault-related deformation are the spatial coincidence of low to intermediate resistivity zones, lateral discontinuity of more resistive blocks, chaotic radar facies, reflector disruption, and signal attenuation. The present geophysical results therefore provide evidence for the shallow geometry and internal deformation structure of the Menanga Fault rather than independently confirming its recent activity. Interpretation of fault activity should be considered together with previous seismicity and geomorphological evidence and, ideally, supported by chronological constraints. Future studies should extend the geophysical survey coverage and integrate structural mapping, paleoseismic trenching, dating of fault-related deposits, and microseismic monitoring to better constrain the geometry, continuity, and activity history of the Menanga Fault.

AUTHOR CONTRIBUTIONS

Conceptualization, RNS, MRS, and BAF; methodology, RNS, MRS, BAF, and INPP; software, RNS, MRS, and DP; validation, RNS, BAF, INPP, and SH; formal analysis, RNS, MRS, BAF, and DP; investigation, RNS, MRS, INPP, SH, DP, DA, SNL, and MDP; resources, RNS, MRS, BAF, and INPP; data curation, RNS, MRS, and DP; writing—original draft preparation, RNS; writing—review and editing, RNS, MRS, BAF, INPP, SH, DP, DA, SNL, and MDP; visualization, RNS, MRS, and DP; supervision, RNS and BAF; project administration, RNS. All authors have read and agreed to the published version of the manuscript.

ACKNOWLEDGMENT

This research is funded by Institut Teknologi Sumatera through Hibah Kepakaran 2025 with contract number: 1998an/IT9.2.1/PT.01.03/2025. The authors would like to thank Dini Wulandari, Fauzan Ahmad, Yelli Monica, Jesika Anastasya Manalu, Adella Sinaga, Endang Sulistiawati, Chandra Laksmana Putra, Delon Alpredo Pardede, Catur Adi Taren, Vira Widya Ningsih, Fadhillah Zeid Akbar, and Cindi Panjaitan for all their contribution in the field survey.

CONFLICTS OF INTEREST

The authors declare no conflict of interest concerning the publication of this article. The authors also confirm that the data and the article are free of plagiarism.

REFERENCES

Adni Pesma, R., & Sitanggang, A. F. (2024). The estimation of fault zone based on 2D geoelectric in Ulujadi, Palu City, Center Sulawesi. JGE (Jurnal Geofisika Eksplorasi), 10(1), 5–15. https://doi.org/10.23960/jge.v9i2.333

Aliyannezhadi, A., Mehrnia, S. R., Kimiagar, S., Rahimi, H., & Sadrmohammadi, N. (2020). Evaluation of GPR method in identification hidden faults of alluvial deposits in north of

Persian Gulf artificial lake, twenty-two district of Tehran. Journal of Applied Geophysics, 179, 104108. https://doi.org/10.1016/j.jappgeo.2020.104108

Argante, V., Tanner, D. C., Brandes, C., von Hagke, C., & Tsukamoto, S. (2022). The memory of a fault gouge: An example from the Simplon Fault Zone (Central Alps). Geosciences, 12(7), 268. https://doi.org/10.3390/geosciences12070268

Duquesnoy, T., Bellier, O., Kasser, M., Sébrier, M., Vigny, C., & Bahar, I. (1996). Deformation related to the 1994 Liwa earthquake derived from geodetic measurements. Geophysical Research Letters, 23(21), 3055–3058. https://doi.org/10.1029/96GL02818

Famiglietti, N. A., Memmolo, G., Memmolo, A., Migliazza, R., Gagliarde, N., Di Bucci, D., Cheloni, D., Vicari, A., & Massa, B. (2025). Low-frequency ground penetrating radar for active fault characterization: Insights from the Southern Apennines (Italy). Remote Sensing, 17(21), 3631. https://doi.org/10.3390/rs17213631

Galli, P. A. C., Giocoli, A., Peronace, E., Piscitelli, S., Quadrio, B., & Bellanova, J. (2014). Integrated near surface geophysics across the active Mount Marzano Fault System (southern Italy): Seismogenic hints. International Journal of Earth Sciences, 103(1), 315–325. https://doi.org/10.1007/s00531-013-0944-y

Hendrawan, R. N., Draniswari, W. A., Bakhtiar, A. Y., & Widiatama, A. J. (2023). Geomorphic indices and fault segmentation indication of Menanga Fault at Pesawaran, Lampung. JGE (Jurnal Geofisika Eksplorasi), 9(3), 184–193. https://doi.org/10.23960/jge.v9i3.287

Hirata, M., Muto, J., & Nagahama, H. (2017). Shear zone development and frictional instability of fault gouge. International Journal of GEOMATE, 12(34), 32–37. https://doi.org/10.21660/2017.34.2660

Jabbar, A., Jabbar, M. K., Jabbar, A., Almasoud, A. S., Akhtar, F., Zulfiqar, M., Mahmood, T., & Rehman, A. (2024). Enhancing radar tracking accuracy using combined Hilbert transform and proximal gradient methods. Results in Engineering, 24, 103479. https://doi.org/10.1016/j.rineng.2024.103479

Lei, X., Ren, J., Xu, X., Qian, R., Zhang, J., & Song, B. (2022). Application of high-power ground-penetrating radar antennas with different frequencies to quickly locate the upper breakpoint of active buried faults in an urban area in the Datong basin (northern China). Journal of Applied Geophysics, 196, 104515. https://doi.org/10.1016/j.jappgeo.2021.104515

Li, C., Wang, Y., Ma, Q., & Wan, X. (2025). Multi-domain feature analysis and application research of GPR aliased signals. Sensors, 25(9), 2741. https://doi.org/10.3390/s25092741

Lockner, D. A., & Byerlee, J. D. (1985). Complex resistivity of fault gouge and its significance for earthquake lights and induced polarization. Geophysical Research Letters, 12(4), 211–214. https://doi.org/10.1029/GL012i004p00211

Mangga, S. A., Amiruddin, Suwarti, T., Gafoer, S., & Sidarto. (1993). Geological map of the Tanjungkarang Quadrangle, Sumatera (Scale 1:250,000). Geological Research and Development Centre.

Monge-Cerda, F. E., Delgado-Rodríguez, O., Ramos-Leal, J. A., & Sánchez-Higueredo, L. E. (2024). Geoelectrical characterization of non-filled active faults in Jaral de Berrios, Guanajuato, México. Journal of Applied Geophysics, 227, 105431. https://doi.org/10.1016/j.jappgeo.2024.105431

Nevedrova, N. N., Deev, E. V., Ponomarev, P. V., & Trofimuk, A. A. (2017). Fault structures and their geoelectric parameters in the epicentral zone of the 27 September 2003 Chuya earthquake (Gorny Altai) from resistivity data. Russian Geology and Geophysics, 58(1), 123–132. https://doi.org/10.1016/j.rgg.2016.01.021

Nurfitriana, I., Nugraha, P., Wulandari, R., Ibrahim F, E., & Wibowo, A. (2022). Identification of the existence of inferred Menanga Fault based on gravity anomaly, Pesawaran, Lampung. In Proceedings of the Soedirman International Conference on Mathematics and Applied Sciences (SICOMAS 2021) (pp. 78–83). Atlantis Press. https://doi.org/10.2991/apr.k.220503.017

Nurfitriana, I., Wibowo, A., & Rudianto, R. (2021). Relokasi gempa bumi swarm di Pesawaran-Lampung, Januari 2021. Jurnal Geocelebes, 5(1), 91–101. https://doi.org/10.20956/geocelebes.v5i1.13328

Pauselli, C., Federico, C., Frigeri, A., Orosei, R., Barchi, M. R., & Basile, G. (2010). Ground penetrating radar investigations to study active faults in the Norcia Basin (central Italy). Journal of Applied Geophysics, 72(1), 39–45. https://doi.org/10.1016/j.jappgeo.2010.06.009

Sellmann, S., Quigley, M., Duffy, B., & Moffat, I. (2022). Ground penetrating radar of neotectonic folds and faults in south-central Australia: Evolution of the shallow geophysical structure of fault-propagation folds with increasing strain. Geosciences, 12(11), 395. https://doi.org/10.3390/geosciences12110395

Sieh, K., & Natawidjaja, D. (2000). Neotectonics of the Sumatran fault, Indonesia. Journal of Geophysical Research: Solid Earth, 105(B12), 28295–28326. https://doi.org/10.1029/2000JB900120